

Comparison of thermal damage calculated using magnetic resonance thermometry, with magnetic resonance imaging post-treatment and histology, after interstitial microwave thermal therapy of rabbit brain

M D Sherar†§¶, J A Moriarty‡, M C Kolios§, J C Chen||, R D Peters‡§,
L C Ang‡, R S Hinks‡, R M Henkelman‡§||, M J Bronskill‡§|| and
W Kucharczyk‡||

† Ontario Cancer Institute/Princess Margaret Hospital, University of Toronto, Canada M5G 2M9

‡ Sunnybrook and Women's College Health Science Center, University of Toronto, Canada

§ Department of Medical Biophysics, University of Toronto, Canada

|| Department of Medical Imaging, University of Toronto, Canada

¶ Department of Radiation Oncology, University of Toronto, Canada

Received 20 December 1999

Abstract. Clinical application of high-temperature thermal therapy as a treatment for solid tumours requires an accurate and close to real-time method for assessing tissue damage. Imaging methods that detect structural changes during heating may underestimate the extent of thermal damage. This is due to the occurrence of delayed damage manifested at tissue locations exposed to temperatures lower than those required to cause immediate structural changes. An alternative approach is to measure temperature and then calculate the expected damage based on the temperature history at each tissue location. Magnetic resonance (MR) imaging methods now allow temperature maps of the target and surrounding tissues to be generated in almost real-time. The aim of this work was to evaluate whether thermal damage zones calculated on the basis of MR thermometry maps measured during heating correspond to actual tissue damage as measured after treatment by histological methods and MR imaging.

Four male rabbits were treated with high-temperature thermal therapy delivered in the brain by a single microwave antenna operating at 915 MHz. MR scanning was performed before, during and after treatment in a 1.5 T whole-body scanner. Temperature maps were produced using the proton resonance frequency (PRF) shift method of MR thermometry. In addition, conventional T_1 -weighted and T_2 -weighted spin-echo images were acquired after treatment. Thermal damage zones corresponding to cell death, microvascular blood flow stasis and protein coagulation were calculated using an Arrhenius analysis of the MR temperature/time course data. The calculated zones were compared with the lesions seen on histopathological examination of the brains which were removed within 6–8 h of treatment.

The results showed that calculated damage zones based on MR thermometry agreed well with areas of damage as assessed using histology after heating was completed. The data suggest that real-time calculations of final expected thermal damage based on an Arrhenius analysis of MR temperature data may provide a useful method of real-time monitoring of thermal therapy when combined with conventional T_2 -weighted images taken after treatment.

1. Introduction

Microwave coagulation therapy is a minimally invasive alternative treatment for tumours. Percutaneous and intraoperative techniques have attracted considerable interest for the

treatment of liver tumours (Sato *et al* 1996, Hamazoe *et al* 1995), recurrent prostate tumours (Lancaster *et al* 1999) and in adjunctive therapy of intracranial meningiomas (Zhou *et al* 1996). In addition several groups have developed transurethral methods for the therapy of benign prostatic hyperplasia (Goldfarb *et al* 1995). These techniques are employed to minimize the side-effects of treatment such as damage to surrounding critical normal tissues (e.g. the rectum in the case of prostate cancer treatments) and to reduce trauma by avoiding major incisions. Dipole and helical coil antennas are available for medical use and are commonly operated at the approved frequencies of 915 MHz or 2450 MHz in the US and at 434 MHz in Europe. Specific characteristics of microwave antennas have been well reviewed in the literature (Tremblay *et al* 1992). The specific absorption rate (SAR) pattern associated with the helical antenna used in these experiments has a three-dimensional tear-drop shape, centred on the antenna tip which is advantageous for localized energy deposition in tissues. These characteristics make the helical coil antenna suitable for thermal coagulation of small tumours.

Widespread clinical use of high-temperature minimally invasive thermal therapy requires accurate real-time assessment of thermal damage to ensure destruction of the target tissue and sparing of surrounding normal structures. This assessment may be achieved in two ways. The first is to directly monitor the structural changes due to heating using diagnostic imaging techniques such as ultrasound (Bush *et al* 1993, Gertner *et al* 1998), magnetic resonance imaging (Anzai *et al* 1995, Schwarzmaier and Kahn 1995, Moriarty 1998) or computed tomography (Harries *et al* 1994). The main problem with these methods is that the final extent of cell death due to heating may extend beyond the zone of damage as assessed by imaging the structural changes that occur when the treatment is being delivered. This is due to the fact that the temperature at which structural changes in tissue occur is higher than the temperatures that can lead to cell death. Stated another way, tissue which shows no evident imaging change during heating, may have received sufficient thermal damage to subsequently die with a latency of 24 h or more. Consequently, depending on the temperature gradient during treatment, the final volume of cell death may be considerably larger than tissue changes visualized during treatment.

An alternative approach to this problem is to calculate the expected volume of cell death based on temperature measurements during heating. The actual level of tissue damage is a function of both temperature and heating time. Given the temperature history at each spatial location, the level of thermal damage can be calculated using an Arrhenius analysis which assumes that some thermal damage processes follow first order reaction rate kinetics. Several endpoints of thermal damage in tissue including cell death, microvascular stasis and protein coagulation can be mathematically modelled using this approach (Skinner *et al* 1998). The use of temperature histories to calculate accumulated thermal damage in tissues has been limited by the sparse data sets provided by invasive temperature probes such as thermocouples, thermistors and fibreoptic thermometers. With the advent of magnetic resonance thermometry (Ishihara *et al* 1995) it is now possible to acquire full three-dimensional temperature data sets. Thus, thermal damage zones corresponding to cell death may be calculated throughout the 3D target and surrounding tissue volume. Similar predictions are possible for other damage measures (e.g. microvascular blood flow stasis) for which the Arrhenius parameters have been derived.

The MR thermometry technique employed involves exploiting the change in the Larmor frequency of protons as a function of temperature (Hindman 1966). The phase of the MR signal, which is dependent on the Larmor frequency, and hence the temperature, is measured to give a three-dimensional map of temperature as a function of time and location in the tissue (Ishihara *et al* 1995). This method of thermometry is relatively independent of tissue type (Peters *et al* 1998), although artefacts related to the orientation of heating sources in the magnetic field do exist (Peters *et al* 1999). Of relevance to this study is the fact that it is possible to use MR

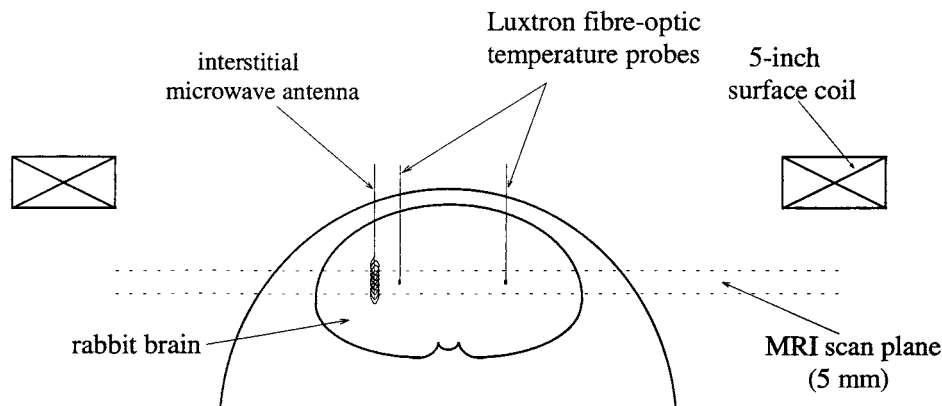


Figure 1. Schematic diagram of the MR imaging and thermal treatment delivery in rabbit brain.

thermometry during microwave heating (Vitkin *et al* 1997). The purpose of the present study is to compare thermal damage zones corresponding to cell death, microvascular collapse and protein denaturation calculated from the thermal history of the tissue, as measured by MR thermometry, with histological sections of the tissue taken after treatment and corresponding post-treatment MR images. The comparison highlights the importance of considering the most appropriate tissue process (cell death, microvascular collapse, protein denaturation) when calculating or measuring the true extent of thermal damage during thermal therapy.

2. Materials and methods

2.1. Animal preparation

Four male New Zealand White rabbits, weighing between 4.8 and 5.8 kg, were used. The animals were cared for according to the Canadian Council for Animal Care Guidelines and approval for this investigation was obtained from the local animal care committee. Anaesthesia was induced with ketamine HCl (50 mg kg⁻¹ intramuscular) and xylazine (5 mg kg⁻¹ intramuscular) and maintained with a cocktail of ketamine (50 mg kg⁻¹) and xylazine (5 mg kg⁻¹) in saline, administered at 30–40 min intervals through an ear vein cannula (2 cm³ intravenous). Dexamethasone (2 mg) was given 24 h prior to therapy (intramuscular) and at induction (intravenous) to reduce brain oedema.

The animals were immobilized in an MR-compatible acrylic frame and three burrholes (2.5 mm) were drilled through the calvarium. The microwave antenna was inserted into the right cerebral hemisphere through the first burrhole. The antenna was enclosed in a thin plastic jacket for cooling with distilled water. A fibreoptic temperature probe was placed through the second burrhole. A second temperature probe was placed in the contralateral cerebral hemisphere, through the remaining burrhole. A schematic diagram of the experimental arrangement is shown in figure 1.

2.2. Tissue heating and temperature measurement

A 915 MHz microwave generator (Dornier, Kennesaw, GA) was positioned outside the scanner room. Power output was set at 20 W at the source. Heating durations were 120, 70 and 100 s for the three rabbits. To reduce MR image artefact, power was delivered to the MR-compatible

antenna through 8 m of coaxial cable via a waveguide into the scanner room. The antenna had a 12 mm × 1 mm (length × diameter) helical emitting element at its tip. During heating the antenna was water-cooled with a flow rate of 40 cm³ min⁻¹. Both interstitial fibreoptic temperature probes were used to collect temperature data at 20 s intervals during each experiment using a Luxtron 3000SL fluoroptic thermometry system (Luxtron, Mountainview, CA).

2.3. Magnetic resonance imaging

Scanning was performed in a 1.5 T whole-body MR scanner (GE SIGNA, General Electric Medical Systems, Milwaukee, WI) with a 5" surface coil. A three-dimensional gradient-echo sequence (TR = 55 ms, TE = 11 ms, flip angle = 30°, matrix = 256 × 256, field-of-view = 8 cm) was used to verify the positions of the antenna and the temperature probes.

A scan plane was chosen, perpendicular to the antenna, at the location of the ipsilateral temperature probe. Images were acquired in this plane using a two-dimensional fast spoiled gradient-echo (FSPGR) sequence (TR = 38.9 ms, TE = 10.0 ms, flip angle = 25°, matrix = 256 × 256, field-of-view = 8 cm, slice thickness = 5 mm) every 20 s (with two signal averages). Ten pretreatment images were obtained to form an average baseline image. Power to the microwave antenna was then turned on. At the completion of the heating phases of the experiment, power was turned off to allow unassisted cooling to occur until the temperature returned to the baseline value. Images were continuously acquired with this FSPGR sequence before, during and after heating. MR signal phase changes corresponding to these FSPGR images were calculated off-line on a Sun Workstation (Sparc Station 5, Sun Microsystems Inc., Mountain View CA). As images were acquired every 10 s data were available for each point in the chosen 2D plane throughout heating and cooling.

Conventional T_1 -weighted (T1W; TR = 500 ms, TE = 20 ms), T_2 -weighted (T2W; TR = 2000 ms, TE = 20, 80 ms) and gadolinium-enhanced (total dose = 1.0 ml or 0.2 ml kg⁻¹) T_1 -weighted spin-echo images were acquired in a scan-plane perpendicular to the antenna immediately after the dynamic imaging sequence was completed. The spatial resolution and slice thickness of the spin-echo sequences were identical to the gradient echo sequence. Delayed spin-echo images were also obtained 3–4 h after heating.

2.4. Specimen collection and pathology

One animal died immediately. At the completion of heating, the remaining animals were maintained under general anaesthesia for 4 and 9 h in order to allow sufficient time for a host response to become manifest. The animals were then sacrificed by intravenous injection of a pentobarbital/propylene glycol mixture (euthanyl 2 ml/4.5 kg intravenously; MTC Pharmaceuticals, Cambridge, Ontario). The brains were removed *in toto* for pathological evaluation within 30 min of the sacrifice. Specimens were fixed immediately in 10% buffered formalin for 48 h. The brains were then sliced to correspond to the imaging scan plane, orthogonal to the tract made by the antenna and the fibreoptic temperature probes. The tissue slices were processed and embedded in paraffin wax. Sections were cut at 8 μm thickness, mounted on glass slides and then stained with haematoxylin-eosin and Luxol fast blue.

Coregistration between MR images and histopathological specimens was determined by visual inspection of the corresponding anatomical features. Each MR image was imported into an image analysis program (ImagePC, Scion Corp., Frederick, MD) and the transverse diameter of the visualized lesion was measured. Corresponding measurements were made in the histopathological specimens. However, because of shrinkage of the tissues due to fixation (16%, 24% and 27% respectively) the scale of the histopathological specimens was adjusted

Table 1. Activation energies and frequency factors for thermal damage in tissue.

Process	Activation energy, E_a (J mol ⁻¹)	Frequency factor, A (s ⁻¹)
Cell death [†]	5.064×10^5	2.984×10^{80}
Microvascular blood flow stasis [‡]	6.67×10^5	1.98×10^{106}
Protein coagulation [§]	2.577×10^5	7.39×10^{37}

[†] Borelli *et al* (1990).

[‡] Brown *et al* (1992).

[§] Jacques *et al* (1991).

upwards so that the length of the major anteroposterior axis of the histopathological specimen was equivalent to that measured on the MR image.

2.5. Thermal model calculations

Temperature histories measured by MR thermometry were used as input into an Arrhenius damage integral to calculate expected volumes of damaged tissue. The general Arrhenius equation describing a chemical process is given by

$$\Omega = \int A e^{-E_a/RT} dt \quad (1)$$

where

$$\Omega = \ln(c(t)/c(0)). \quad (2)$$

Here, $c(t)$ is the concentration of final product at time t , and $c(0)$ is the concentration of final product at time $t = 0$, E_a is the activation energy for the transition, A is the frequency factor and R is the universal gas constant. This formalism can be applied to several measures of thermal damage in tissue. For example, $c(t)$ can describe the proportion of cells killed, collapsed blood vessels or protein molecules coagulated. For each process, a particular activation energy and frequency factor will apply. These constants are available from experimental data for the processes of interest as shown in table 1 (see Skinner *et al* (1998) for details of their calculation). The activation energy and frequency factor for cell death were determined from families of cell survival curves for baby hamster kidney cells exposed to elevated temperatures up to a maximum of 57 °C as a function of time (Borelli *et al* 1990). The Arrhenius parameters corresponding to microvascular blood flow stasis in response to heat were derived from measurements of changes in blood flow when muscle tissue was heated to temperatures up to 47 °C (Brown *et al* 1992). Arrhenius parameters for protein coagulation in liver tissue were measured by Jacques *et al* (1991) using changes in tissue optical properties as the indicator of protein coagulation. In all cases we assumed the Arrhenius parameters (shown in table 1) to be constant over the entire temperature range measured during the experiment.

3. Results

Temperature and MR phase change measured as a function of time at the ipsilateral fiberoptic thermometer position are shown in figure 2(a) for a typical animal. The distances to the ipsilateral temperature probes were 5 mm, 5 mm and 6 mm respectively in the three animals. In the example shown in figure 2(a) the temperature at this position reached a maximum of 71 °C at a time of 70 s after the power was turned on. The power was then switched off. Consequently, the temperature dropped rapidly to below 40 °C at this location after another

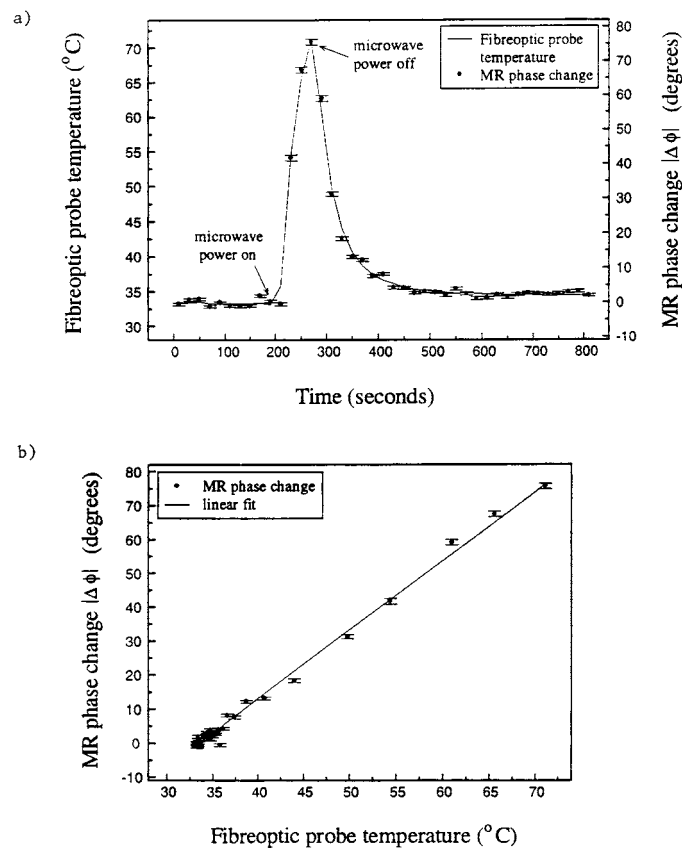


Figure 2. (a) MR phase change and fiberoptic temperature measured as a function of time at the ipsilateral temperature probe, during treatment. (b) MR phase change as a function of the temperature measured at the ipsilateral temperature probe at each MRI measurement time point during treatment. Data from both heating and cooling phases is included. Note that no hysteresis is observed.

100 s. MR signal phase changes measured at this location during tissue heating and cooling were used to calibrate the MR thermometry. Hence, temperatures could be ascribed to each point in the 2D plane for each image acquired with the gradient echo sequence during the experiment. The calibration curve shown in figure 2(b) shows that in rabbit brain a good linear fit of phase change with temperature is observed with no hysteresis. As images were recorded every 20 s a thermal history was available for each spatial location in this 2D plane during the experiment.

These data yielded a proton resonance frequency (PRF) shift thermal coefficient of -0.0088 ± 0.0001 (SD) ppm °C⁻¹. Subsequent studies have indicated that this somewhat low value may be due to volume averaging of the temperature distribution within the slice thickness (5 mm). Also, similar experiments have shown the calibration to be extremely sensitive to the location and shape of the region of interest used to measure the temperature-induced phaseshift due to the large thermal gradients present near the heating antennas. Finally, with the microwave antenna oriented perpendicularly to the main magnetic field, magnetic susceptibility related effects can lead to a spatially variable PRF-shift coefficient. These effects are discussed in more detail elsewhere (Peters *et al* 1999).

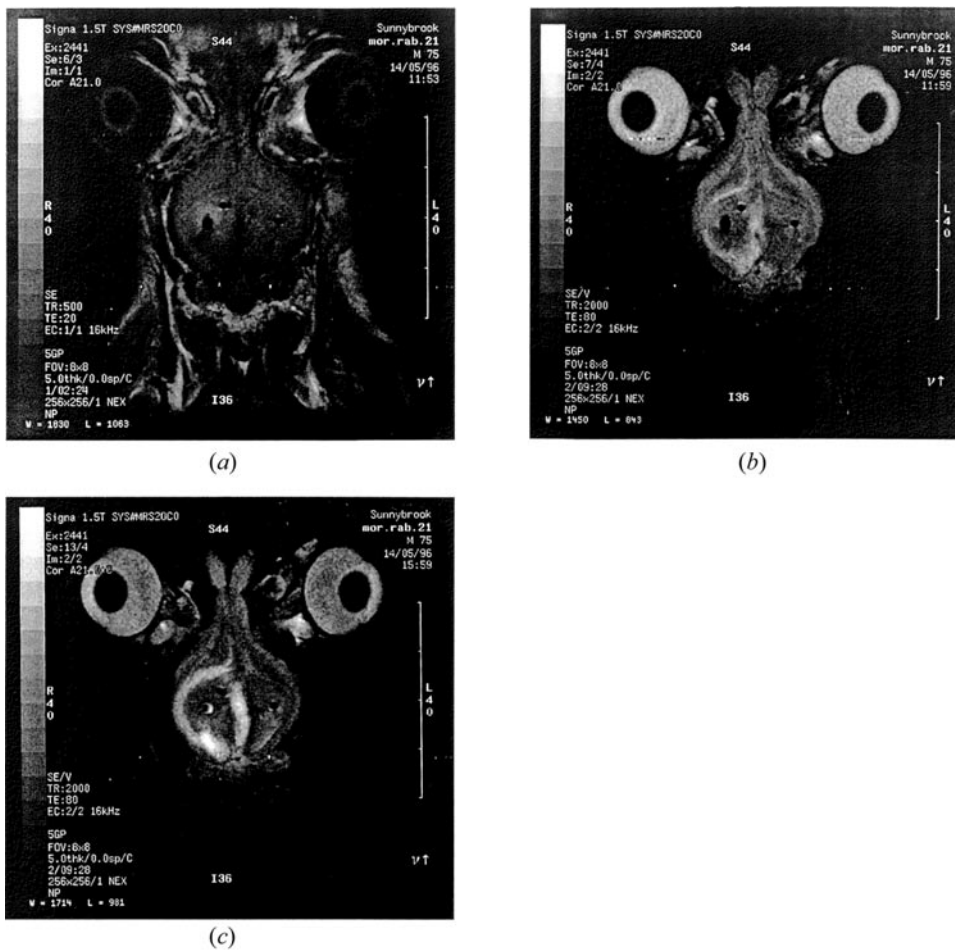


Figure 3. (a) T_1 - and (b) T_2 -weighted image taken at the end of treatment after power had been switched off. (c) T_2 -weighted image taken 4 h later.

T_1W and T_2W images taken within 30 min of the power being turned off are shown in figure 3 together with a T_2W image taken 4 h later. Previous authors (Moriarty *et al* 1998) have described the MR imaging characteristics of thermal damage due to interstitial microwave heating. These consist of a high-signal zone immediately adjacent to the antenna and a less well visualized low-signal outer zone on T_1W images. T_2W images show opposite but more easily visualized contrast.

An MR phase image resulting from the FSPGR sequence applied at the end of the power on period sequence is shown in figure 4 in the same orientation as the images in figure 3. The accumulated phase is shown to be high adjacent to the antenna, as expected. These images were recorded every 20 s giving a thermal history at each spatial location.

Using the calculated temperature data from the FSPGR sequence, Arrhenius damage integrals were calculated for the three biological processes of interest using equation (1). Figure 5 shows damage images for cell death, microvascular blood flow stasis and protein coagulation for the image plane shown in figures 3 and 4. The calculations were performed over the area of interest outlined by the $3\text{ cm} \times 3\text{ cm}$ white box shown in figure 4. The diameters

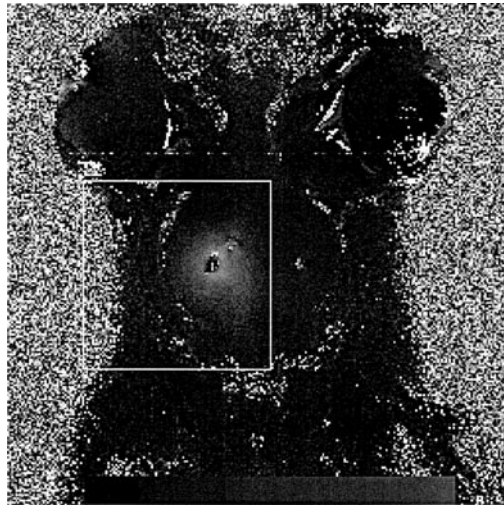


Figure 4. MR FSPGR phase image taken just before power-off. The plane of imaging corresponds to the plane shown in figure 3. White corresponds to a phase change of 360° while black corresponds to zero phase change. Mottled areas correspond to regions where noise dominates the phase measurement. The white box ($3\text{ cm} \times 3\text{ cm}$) corresponds to the area over which Arrhenius calculations of thermal damage were performed (see figure 5).

of damage calculated using $\Omega = 4.6$ (this corresponds to 1% cell survival, blood vessels intact, or uncoagulated protein) were 17 mm (cell survival), 17 mm (microvascular stasis) and 11 mm (protein coagulation).

Damage contours corresponding to 99% cell death and 99% protein coagulation taken from figures 5(a) and 5(c) respectively were overlaid on the corresponding T2W image taken immediately after treatment as shown in figure 6. It was observed that the extent of protein coagulation corresponded with the inside of the high-signal region in the T2W image. Similarly, the extent of the thermal lesion as predicted by the 99% cell death contour corresponded to the outer edge of the high-signal zone.

The ability of the Arrhenius theory to correctly predict damage was determined by comparing the measurements from figure 5 with the size of the thermal lesions seen on histopathological examination. The whole mount of the brain is shown in figure 7. The thermal lesion can be seen in the right cerebral hemisphere. A central defect corresponds to the tract left by the antenna. Grossly, the lesion measured approximately 11 mm in diameter and was roughly circular in appearance. This is in agreement with the diameter of coagulation as predicted by the Arrhenius analysis. Tissues within the lesion were paler on gross examination than those in the opposite cerebral hemisphere.

Microscopically, a central tract was identified at the site of the antenna in each of the three animals. Surrounding the antenna a region of coagulation was seen which was variable in size. The appearance varied from an acellular region with focal areas of haemorrhage to that of charred tissue. In some specimens, cells immediately adjacent to the antenna tract were not as severely affected in appearance, presumably due to the protective effect of the antenna cooling mechanism. More peripheral tissues exhibited varying degrees of necrosis. Cells containing fragmented nuclei (karyorrhexis) were observed closest to the central coagulated region. Further from the antenna, cell nuclei were small (pyknosis) and pink neurons were observed consistent with early necrosis. Vascular congestion and oedema increased towards the

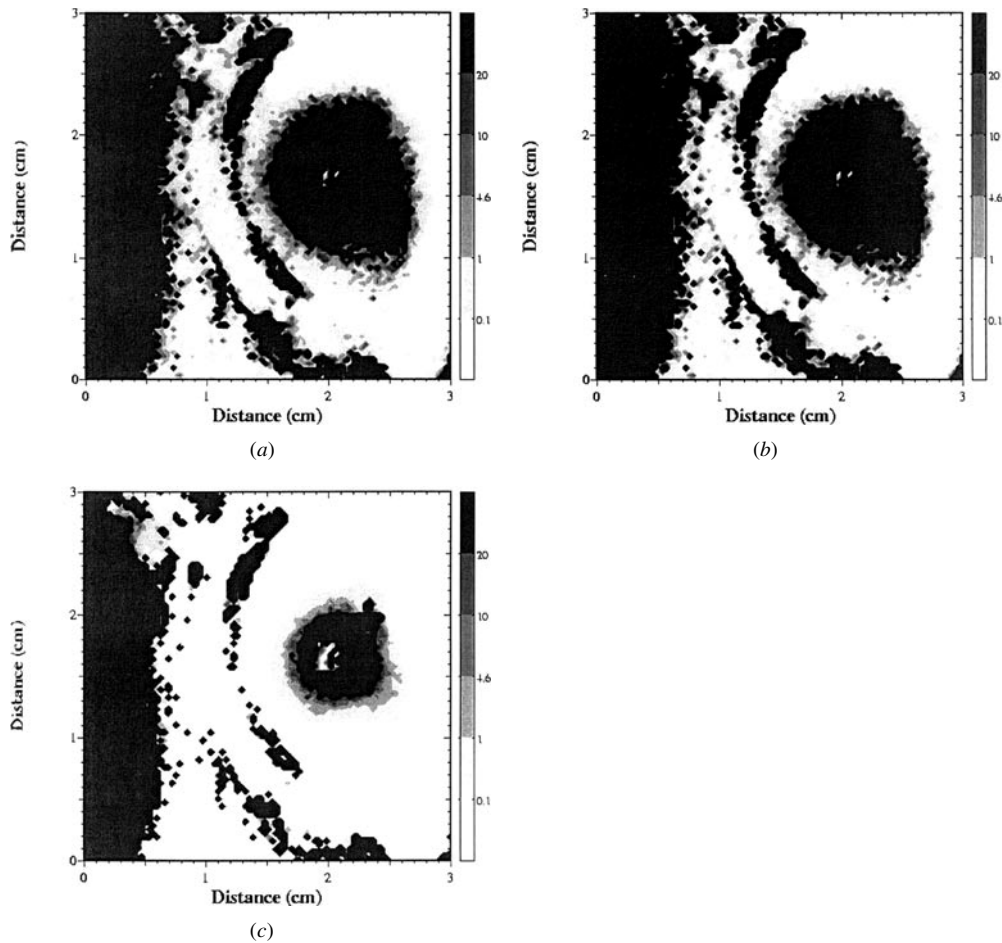


Figure 5. Contours of thermal damage corresponding to $\Omega = 0.1, 1.0, 4.6, 10.0$ and 20.0 calculated from equation (1) using the MR temperature history measured at each spatial location in the vicinity of the microwave antenna. The area of calculation corresponds to the white box in figure 4. Damage corresponding to (a) cell death, (b) microvascular blood flow stasis and (c) protein coagulation is shown. The Arrhenius parameters for each measure of damage were derived from the literature (table 1). The contour corresponding to $\Omega = 4.6$ was used for measurements of areas of thermal damage as it corresponds to 99% cell kill, blood flow stasis or protein coagulated for each respective Arrhenius calculation.

perimeter of the necrotic region identified on histopathological examination. Correspondence between the diameter of the thermal lesion seen on histopathology and that measured from T2W MR images is documented in table 2. The Arrhenius calculations for the three thermal damage endpoints of interest based on MR thermometry are compared with these measurements for the three rabbits in table 2.

4. Discussion

The calculation of thermal damage based on temperatures measured during high temperature thermal therapy has had two major limitations. First, until the advent of MR thermometry only sparsely sampled temperature data sets were available requiring invasive

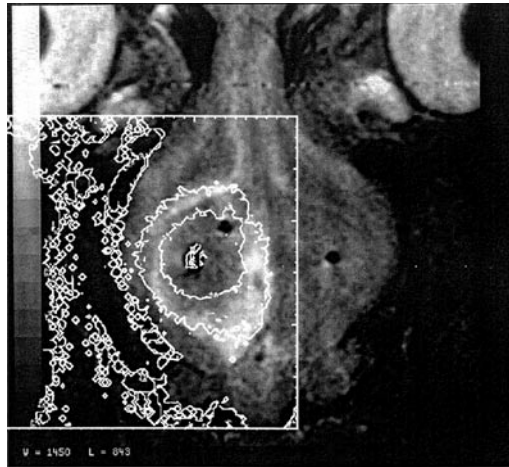


Figure 6. T_2 -weighted image taken immediately after treatment (same as figure 3(c)) with Arrhenius calculations of thermal tissue damage corresponding to 99% cell death and 99% protein coagulated superimposed.



Figure 7. Histological section of the plane corresponding to the images shown in figure 5.

needle-based thermometers. Therefore, the estimation of full three-dimensional thermal damage zones was often inaccurate. The second limitation concerns the theory that is used to calculate thermal damage based on the temperature history at each location in the tissue.

Table 2. Thermal lesion diameters (mm) measured using T_2 -weighted MR images both immediately after treatment and at 4 h post-treatment, histopathology, or calculated using MR thermometry-based Arrhenius analyses for three damage endpoints; cell death (CD), microvascular stasis (BF) and protein coagulation (CO). For the Arrhenius calculations, the diameters were calculated assuming a damage threshold of 99% (or 1% survival of cells, microvasculature or native protein respectively).

Experiment	Immediate T_2 image	4 h delayed T_2 image	Histopathology	Arrhenius analysis		
				CD	BF	CO
Rabbit #1	14	15	14	14	14	8
Rabbit #2	14	15	15	17	17	11
Rabbit #3	16	16	16	16	16	13

Most of the available data that can be used to derive Arrhenius parameters for the tissue changes we have studied, particularly cell death and microvascular blood flow stasis, is based on measurements in tissue and cell cultures exposed to relatively low temperatures (57 °C and 47 °C respectively). Experiments to measure these parameters at high temperatures would be extremely difficult to conduct due to the very short controlled time exposures that would be required. The question then arises as to whether the Arrhenius parameters derived from data measured at low temperatures are applicable to high temperature thermal therapy.

The results of this experiment demonstrated that the size of the central area of coagulation as seen on the gross specimen was accurately predicted by the Arrhenius calculation using a threshold of $\Omega = 4.6$ corresponding to 99% of protein coagulated. Similarly the diameter of the thermal lesion identified on the histological specimen corresponded to the Arrhenius calculation of cell death again assuming a threshold of $\Omega = 4.6$ (corresponding to 99% cell death or 1% cell survival). In all three Arrhenius calculations, the predicted size of the area of thermal damage is relatively insensitive to which threshold value of Ω is used. This is due to the very large temperature gradients that occur during interstitial thermal therapy combined with the exponentially varying dependence of damage on temperature. This sharp threshold phenomenon has been observed experimentally both here and by others as a very clearly distinguished boundary between viable and non-viable tissue. The large temperature gradient also results in damage boundaries corresponding to cell death and microvascular blood flow stasis being almost equal, despite the fact that the critical temperatures (arbitrarily defined as the constant temperature for which 10 min of exposure leads to a damage $\Omega = 1$, or 63% damage) for these two processes differ by approximately 2 °C. However, the results do show that if one uses the area of coagulation as a measure of tissue damage this will significantly underestimate the true area of cell death. This is because the critical temperature for protein coagulation (approximately 60 °C) is much higher than for cell death or microvascular stasis.

The use of rodent cell data to derive Arrhenius parameters for cell death was based on the existence of cell survival curves measured at high temperatures (Borelli *et al* 1990). It is well known that at low temperatures rodent cells and human cells can have quite different cell sensitivities. As discussed previously, due to the exponential relationship of cell death with temperature and the large temperature gradients observed during interstitial thermal therapy, the variation in thermal sensitivity of cells to heat damage is predicted to have only a small effect on the predicted size of the thermal lesion. However, it is instructive to compare contours of damage based on the rodent cell *in vitro* data with a more general definition of thermal dose. We calculated thermal dose contours for these treatments based on the Sapareto/Dewey formalism (Sapareto and Dewey 1984). Threshold doses of 240 and 10^9 equivalent minutes at 43 °C were found to correspond very closely to the contours of cell death and protein coagulation respectively, shown in figure 6.

The present experiments were restricted to the acute changes resulting from microwave thermal therapy in normal rabbit brain. Signal characteristics seen with MRI correspond to those which have been described previously in the literature (Moriarty *et al* 1998). MR images demonstrate two zones: an inner zone, which is hyperintense on T1W images and iso/hypointense on T2W images, and an outer zone around which T1W images frequently show ring enhancement. However, discrete ring enhancement was not a marked feature in the three animals in this study. The contrast seen on T1W images is inversely related to that seen on T2W images. Therefore, the diameter of the thermal lesion seen on MRI in these experiments was determined on the basis of the T2W images, along the olfactory tracts, in the region of the corpus callosum or adjacent to the fiberoptic temperature probes in the contralateral hemisphere. Necrosis was not identified in these areas on histological examination. The findings probably represent vasogenic oedema and, hence, these regions were not included in measurements of the diameter of the primary lesion. Oedema was minimized in this study by the prior administration of dexamethasone. The observation that the areas of cell death based on an Arrhenius model correspond well with the outer edge of the hyperintense zone as observed on T2W images is consistent with previous studies (Anzai *et al* 1992). This indicates that surrogate markers of damage based on T2W images may play a useful role in predicting tissue damage if MR thermometry is not available. However, caution must be applied due to the change in size of the lesion observed on T2W images with time after treatment (Farahani *et al* 1995).

Several limitations of the procedure outlined above for comparison of the MR images and the histopathological specimens require clarification. Firstly, exact alignment of the images was not possible as coregistration techniques were not used in this study. A slight change in the shape of the contour of the brain was also identified when it was released from the restrictive confines of the calvarium. Furthermore, initial brain swelling was later replaced by shrinkage during processing. This fixation artefact necessitated the application of a linear correction factor when measuring the diameter of the lesion on the histopathological specimen.

The histopathological characteristics of the thermal lesion were similar for all rabbits. A coagulated region was observed centrally. More peripherally, cells exhibited varying degrees of necrosis with karyorrhectic or pyknotic nuclei. The features suggest decreasing severity of cell death as distance from the antenna increased. Measured diameters of the lesions on histopathological examination included all of these regions.

Tissue characterization available from standard spin-echo images is limited. Lesions may be either bright or dark relative to normal brain tissue. These signal characteristics are insufficient to provide a one-to-one correspondence with the spectrum of histopathological features seen. However, the degree of thermal damage seen on histopathology was greater in the central part of the lesion corresponding to the inner zone on MRI which is hyperintense on T1W images and iso/hypointense on T2W images. Increased vascular congestion was more apparent, corresponding to the outer zone on MRI where the contrast was reversed. However, necrosis was also seen in this region. In some animals shrunken cells, which could still be viable were identified within this region. As the examination of histopathological specimens is not an absolute measure of tissue viability in an individual cell, the potential viability of individual cells should be recognized, particularly when microwave coagulation therapy is employed for the treatment of malignant disease. In several animals a small layer of cells close to the antenna showed less severe thermal damage than more distant regions. This layer was not resolved on MRI. Cytoprotection in this layer was attributed to the thermal protection afforded by water flowing in the adjacent cooling jacket. Failure to achieve cytotoxic temperatures has also been reported adjacent to a cooled RF electrode (Goldberg *et al* 1996). Hence, if microwave thermal therapy is being undertaken for tumour ablation, water flow should be stopped for a

short period at the end of therapy to allow cytotoxic temperatures to be achieved adjacent to the antenna.

5. Conclusion

MRI can delineate the extent of the acute thermal lesion and results show that the size of the region of tissue necrosis measured on histological examination corresponds well with the lesion seen on post-treatment MRI and with Arrhenius calculations of cell death using MR thermometry. Thus real-time monitoring may be used as a predictor of tissue damage during high temperature interstitial thermal therapy.

Acknowledgments

This work was a collaboration between the Ontario Cancer Institute/Princess Margaret Hospital and the Image Guided Minimally Invasive Therapy (IGMIT) project at the University of Toronto. IGMIT is a partnership of Sunnybrook Health Science Centre, The Toronto Hospital, General Electric Medical Systems of Canada and ISG Technologies, that receives significant funding from Technology Ontario as well as from the partners. Funding from the National Cancer Institute with funds from the Terry Fox Run and The Canadian Cancer Society is also gratefully acknowledged. We would like to thank Dornier Medical Systems for providing the microwave antenna and ancillary apparatus used in these experiments and Don Plewes for helpful advice. Also, we thank John Watts, Jennifer Glen, Carrie Purcell and Beverley Young (of SD Laboratories) for their technical support and Anna Sergiou for assistance in preparing the manuscript.

References

- Anzai Y, Lufkin R, DeSalles A, Hamilton DR, Farahani K and Black K L 1995 Preliminary experience with MR-guided thermal ablation of brain tumors *Am. J. Neuroradiol.* **16** 39–48
- Anzai Y, Lufkin R B, Hirschowitz S, Farahani K and Castro D J 1992 MR imaging-histopathologic correlation of thermal injuries induced with interstitial Nd:YAG laser irradiation in the chronic model *J. Magn. Reson. Imaging* **2** 671–8
- Borelli M J, Thompson L L, Cain C A and Dewey W C 1990 Time-temperature analysis of cell killing of BHK cells heated at temperatures in the range of 43.5 °C to 57.0 °C. *Int. J. Radiat. Oncol. Biol. Phys.* **19** 389–99
- Brown S L, Hunt J W and Hill R P 1992 Differential thermal sensitivity of tumour and normal tissue microvascular response during hyperthermia *Int. J. Hyperth.* **8** 501–14
- Bush N L, Rivens I, ter Haar G R and Bamber J C 1993 Acoustic properties of lesions generated with an ultrasound therapy system. *Ultrasound Med. Biol.* **19** 789–801
- Farahani K, Mischel P S, Black K L, De Salles A A, Anzai Y and Lufkin R B 1995 Hyperacute thermal lesions: MR imaging evaluation of development in the brain *Radiology* **196** 517–20
- Gertner M R, Worthington A E, Wilson B C and Sherar M D 1998 Ultrasound imaging of thermal therapy in *in vitro* liver *Ultrasound Med. Biol.* **24** 1023–32
- Goldberg S N, Gazelle G S, Solbiati L, Rittman W J and Mueller P R 1996 Radiofrequency tissue ablation: increased lesion diameter with a perfusion electrode *Acad. Radiol.* **3** 636–44
- Goldfarb B, Bartkiw T and Trachtenberg J 1995 Microwave therapy of benign prostatic hyperplasia *Urol. Clin. N. Am.* **22** 431–9
- Hamazoe R, Hiroka Y, Ohtani S, Hatoh T and Kaibara N 1995 Intraoperative microwave tissue coagulation as treatment for patients with nonresectable hepatocellular carcinoma *Cancer* **75** 794–800
- Harries S A, Amin Z, Smith M E F, Lees W R, Cooke J, Cook M G, Scurr J H, Kissin M W and Brown S G 1994 Interstitial laser photocoagulation as a treatment for breast cancer *Br. J. Surg.* **81** 1617–19
- Hindman J C 1966 Proton resonance shift of water in gas and liquid states *J. Phys. Chem.* **44** 4582–92
- Ishihara Y, Calderon A, Watanabe H, Okamoto K, Suzuki Y, Kuroda K and Suzuki Y 1995 A precise and fast temperature mapping method using water proton chemical shift *Magn. Reson. Med.* **34** 814–23

- Jacques S L, Newman C and He X Y 1991 Thermal coagulation of tissues: liver studies indicate a distribution of rate parameters, not a single rate parameter, describes the coagulation process *Advances in Biological Heat and Mass Transfer* ed J McGrath (New York: ASME) pp 71–3
- Lancaster C, Toi A and Trachtenberg J 1999 Interstitial microwave thermoablation for localized prostate cancer *Urology* **53** 828–31
- Moriarty J A, Chen J C, Purcell C M, Ang L C, Hinks R S, Peters R D, Henkelman R M, Plewes D B, Bronskill M J and Kucharczyk W 1998 MRI monitoring of interstitial microwave-induced heating and thermal lesions in rabbit brain *in vivo* *J. Magn. Reson. Imaging* **8** 128–35
- Peters R D, Hinks R S and Henkelman R M 1998 *Ex vivo* tissue-type independence in proton-resonance frequency shift MR thermometry *Magn. Reson. Med.* **40** 454–9
- 1999 Heat-source orientation and geometry dependence in proton-resonance frequency shift magnetic resonance thermometry *Magn. Reson. Med.* **41** 909–18
- Sapareto S A and Dewey W C 1984 Thermal dose determination in cancer therapy *Int. J. Radiat. Oncol. Biol. Phys.* **10** 787–800
- Sato M, Watanabe Y, Ueda S, Iseki S, Abe Y, Sato N, Kimura S, Okubo K and Onji M 1996 Microwave coagulation therapy for hepatocellular carcinoma *Gastroenterology* **110** 1507–14
- Schwarzmaier H J and Kahn T 1995 Magnetic resonance imaging of microwave induced tissue heating *Magn. Reson. Imaging* **8** 128–35
- Skinner M G, Iizuka M N, Kolios M C and Sherar M D 1998 A theoretical comparison of energy sources—microwave, ultrasound and laser—for interstitial thermal therapy *Phys. Med. Biol.* **43** 3535–47
- Trembly B S, Ryan T P and Stronbehn J W 1992 Physics of microwave hyperthermia *Hyperthermia and Oncology* vol 3, ed M Urano and E Double (Utrecht: VSP) pp 11–98
- Vitkin I A et al 1997 Magnetic resonance imaging of temperature changes during interstitial microwave heating: A phantom study *Med. Phys.* **24** 269–77
- Zhou X P, Xie Q L, Liu J M, Yue Z J and Cai K H 1996 Resection of meningiomas with implantable microwave coagulation *Bioelectromagnetics* **17** 85–8